Journal of Alloys and Compounds 793 (2019) 564–575

Contents lists available at ScienceDirect

Journal of Alloys and Compounds

journal homepage: http://www.elsevier.com/locate/jalcom

# Study of hydrogen storage and electrochemical properties of $AB_2$-type $Ti_{0.15}Zr_{0.85}La_{0.03}Ni_{1.2}Mn_{0.7}V_{0.12}Fe_{0.12}$ alloy

Alexei A. Volodin [a, b], Roman V. Denys [b, c], ChuBin Wan [b, d], Ika Dewi Wijayanti [b, e, f], Suwarno [f], Boris P. Tarasov [a], Vladimir E. Antonov [g], Volodymyr A. Yartys [b, e, *]

[a] Institute of Problems of Chemical Physics RAS, Chernogolovka, 142432, Russia
[b] Institute for Energy Technology, P.O. Box 40, Kjeller, NO-2027, Norway
[c] HYSTORSYS AS, P.O. Box 45, Kjeller, NO-2027, Norway
[d] University of Science and Technology Beijing, 100083, China
[e] Norwegian University of Science and Technology, Trondheim, Norway
[f] Department of Mechanical Engineering, Sepuluh Nopember Institute of Technology (ITS), Surabaya, Indonesia
[g] Institute of Solid State Physics RAS, Chernogolovla, 142432, Russia

ARTICLE INFO

*Article history:*
Received 6 December 2018
Received in revised form
6 March 2019
Accepted 7 March 2019
Available online 9 March 2019

*Keywords:*
Hydrogen storage materials
$AB_2$ laves type intermetallics
Ni-MH batteries
Metal hydride anode
Hydrogen diffusion

ABSTRACT

A C15 $AB_2$ Laves-type $Ti_{0.15}Zr_{0.85}La_{0.03}Ni_{1.2}Mn_{0.7}V_{0.12}Fe_{0.12}$ alloy was prepared by arc melting and annealing. Phase-structural composition, microstructure, hydrogen absorption-desorption properties, thermodynamic and electrochemical performances were characterized by X-ray diffraction, scanning electron microscopy, hydrogen absorption-desorption measurements and electrochemical characterization and were related to the use of the alloys as metal hydride battery anodes.

The alloy contains a C15 FCC intermetallic compound as the main phase and a LaNi secondary phase as the minor constituent (~1 wt%).

During the electrochemical tests, the anode electrodes quickly, after just a few activation cycles, reached a maximum discharge capacity. This was related to the catalytic effect of the La-rich secondary phase which acted as a catalyst of hydrogen absorption-desorption.

Annealing resulted in increase of the maximum discharge capacity from 345 mAh/g for the as cast alloy to 370 mAh/g. Furthermore, the annealed alloy showed a better high rate dischargeability and a higher cyclic stability. After 100 cycles with 100% DOD at discharge current density of 1C, the discharge capacity of the annealed alloy was very high, at a level of 90% of the initial capacity.

The rates of hydrogen diffusion have been characterized by Potentiostatic Intermittent Titration Technique and Electrochemical Impedance Spectroscopy. With increasing an extent of transformation into the hydride, the H diffusion rate in the bulk of the alloy particles decreased. The maximum value of $D_H$ measured by PITT for the annealed alloy was observed for the nearly fully discharged electrode, (SOC 2%).



## 1. Introduction

Currently, $AB_5$-, $A_2B_7$-, $AB_3$- and $AB_2$-type multicomponent metal hydride alloys are extensively studied as anodes of the Ni-MH batteries [1]. $AB_2$-type alloys in many aspects are advantageous as compared to the other alloys [2,3]. Due to the optimised design of the $AB_2$ alloys, during the hydrogen sorption-desorption the crystal lattice volume variations keep the cubic symmetry unchanged, thus reducing the strains and decreasing hysteresis between the pressures of hydrogen absorption and desorption and overpotential of charge and discharge for the metal hydride anode electrode. A smaller hysteresis assists in decreasing energy losses and in improving energy efficiency [4]. One example of $AB_2$ alloy with high H storage capacity is $ZrV_2$ intermetallic compound storing 4.8 at. H/f.u. (2.43 wt% H) at 1 bar $H_2$ [5]. However, at room temperature the formed hydride has a very low equilibrium pressure of hydrogen desorption of $10^{-8}$ bar and thus it cannot be used as a metal hydride anode material.

* Corresponding author. Institute for Energy Technology, P.O. Box 40, Kjeller, NO-2027, Norway.
*E-mail address:* volodymyr.yartys@ife.no (V.A. Yartys).

https://doi.org/10.1016/j.jallcom.2019.03.134
0925-8388/

The alloys with attractive electrochemical properties should have a pressure of hydrogen sorption-desorption below 1 bar at ambient conditions, allowing to reach a high reversible electrochemical capacity. Such pressures can be achieved by a proper selection of the chemical composition of the alloys.

One significant problem with the use of Zr- and Ti-based $AB_2$ alloys is in their difficult activation requiring a long activation process. Thus, improvement of the activation behaviors is a very important issue towards applications of metal hydrides as anode materials of the Ni-MH batteries.

Typically, battery anode $AB_2$-type alloys consist of Zr and Ti on the A site together with a variable combination of transition metals, including V, Cr, Mn, Ni and Fe on the B site [6]. Up till now, the effect of various additives on hydrogen absorption-desorption and electrochemical properties of the $AB_2$ alloys such as Titanium [7,8], Lanthanum [9], Yttrium [10,11], Cerium [12], Praseodymium [13], Neodymium [14], Nickel [15], Molybdenum [16,17], Zinc [18], Aluminum [19], Manganese [20], Vanadium [21], Iron [22,23], Silicon [24] has been extensively studied and documented in the reference publications.

Laves type $AB_2$ alloys predominantly crystallize with structures of two types, a C15 FCC $MgCu_2$ type and a C14 hexagonal $MgZn_2$ type [2]. Analysis of the available reference data leads to a conclusion that C14-predominated MH alloys are more suitable for high-capacity and long-life time applications, while C15-predominated MH alloys provide improved high-rate and low-temperature performances [2,3]. Therefore, many studies are aimed at optimizing the composition of C14/C15 Laves type alloys as H storage and battery electrode materials [25,26], and these works include the use of various mixtures of intermetallic compounds with different structures [27], and the development of activation methods [28] to increase the H storage capacity and to improve the hydrogenation-dehydrogenation kinetics. In addition, the sensitivity of $AB_2$ alloys to gaseous impurities should be addressed [29] together with improvement of their performance in metal-$H_2$ interactions at subzero temperatures (down to − 40 °C) [30].

In the present study we have prepared arc melted $Ti_{0.15}Zr_{0.85}La_{0.03}Ni_{1.2}Mn_{0.7}V_{0.12}Fe_{0.12}$ $AB_2$-type alloy and performed detailed studies of its phase composition and microstructure, including the effect of the annealing, on hydrogen absorption-desorption and electrochemical properties. The objective of the present work was to study electrochemical performance of the predominantly C15 type phase, which was obtained during the annealing. In addition, we used La as a catalyst to facilitate the process of electrochemical exchange. The obtained results are discussed in comparison with the available reference data.

The composition $Ti_{0.15}Zr_{0.85}La_{0.03}Ni_{1.2}Mn_{0.7}V_{0.12}Fe_{0.12}$ was selected based on our in-house research of $AB_2$-type alloys for their application as hydrogen storage materials. The studied alloy showed excellent hydrogen sorption properties (high reversible storage capacity, easy activation, fast kinetics and low hysteresis of isotherms of hydrogen absorption-desorption) which suggested that it could be very promising for its electrochemical applications as well.

As a starting point in the development of this composition we have used the data which was reported for the $Zr_{1-x}Ti_xNi_{1.3}Mn_{0.7-y}V_y$ alloys by Yoshida and Akiba [31]. They showed the use of a multicomponent substitution is an effective method to improve hydrogen storage properties of $AB_2$ alloys. Simultaneous substitution by Ti on Zr site and by V on the Mn site in a C15-type $ZrNi_{1.3}Mn_{0.7}$ phase alloy allowed to control the level of plateau pressures and to reduce hydrogen absorption/desorption hysteresis. As hysteresis leads to the energy loss during absorption/desorption cycle, in MH electrodes it causes voltage overpotential during the charging of the anode.

We have optimised composition of the alloys to obtain a flat and broad pressure plateau with a minimum value of hysteresis. Selection of optimised composition of our alloy allowed to reach the following benefits: proper choice of Ti/Zr ratio tuned the values of the plateau pressures; vanadium substitution reduced hysteresis while small addition of Fe resulted in flat plateaux and increased the values of the reversible H storage capacities.

## 2. Experimental

The $Ti_{0.15}Zr_{0.85}La_{0.03}Ni_{1.2}Mn_{0.7}V_{0.12}Fe_{0.12}$ alloy was prepared by arc melting of the starting elemental metals with a purity of not less than 99.7% in argon atmosphere. Manganese was taken in 4 wt% excess to compensate for its evaporation loss during the melting. As-cast alloy ingot was crushed and enclosed into a sealed stainless steel tube sample holder. The sealing was performed in argon gas. Subsequently the sample was annealed at 950 °C for 16 h and quenched into cold water after the annealing. The elemental composition of the obtained alloys was analyzed using EDX analysis. According to this analysis, the elemental composition of the alloys corresponded to the gross formula $Ti_{0.15}Zr_{0.85}La_{0.03}Ni_{1.2}Mn_{0.7}V_{0.12}Fe_{0.12}$.

X-ray diffraction (XRD) study with $CuK_{\alpha 1}$ radiation was used to identify the phase structure and composition of the alloys. The XRD data were collected using Siemens D500 BRAUN diffractometer. Powder diffraction data were analyzed by Rietveld whole-profile refinements method using the General Structure Analysis System (GSAS) software [32].

The surface morphology and phase composition of the alloys were analyzed using TESCAN VEGA II XMU Scanning Electron Microscope (SEM) with OXFORD INCA X–Sight EDX Detector. The samples were embedded into SpeciFix Resin (Struers), dried and polished. The backscattered electron (BSE) imaging mode was used to characterize the phase-structural composition and morphology of the prepared alloys at NTNU.

The isotherms of hydrogen absorption and desorption by the $Ti_{0.15}Zr_{0.85}La_{0.03}Ni_{1.2}Mn_{0.7}V_{0.12}Fe_{0.12}$ alloy were measured using a PCT setup. Annealed alloy powder was placed into a thermostated autoclave. The samples were activated in vacuum at 250 °C for 30 min. Then one cycle of full hydrogen absorption-desorption was performed. The hydrogen absorption-desorption isotherms were measured after the alloy's activation. The measurements were performed at 20, 50 and 80 °C (293, 323 and 353 K).

For the preparation of the MH electrodes, the annealed alloy was first ground and the fraction of the powder with a particle size of 40–60 μm and with average of around 50 μm was separated for the preparation of the anodes. Pellet type MH electrodes were prepared by mixing a MH alloy powder with carbonyl Ni powder having a specific surface area of ~0.7 $m^2$/g. The mixture contained 100 mg of the alloy and 400 mg of carbonyl Ni powder. The pellet electrodes of 10 mm in diameter with a thickness of approximately 1 mm were fabricated by cold-pressing under a pressure of 12 MPa for 5 min. Then the pellet was placed between the two Ni foam plates.

Electrochemical measurements were performed at room temperature using a three-electrode cell with a 9 M aqueous KOH electrolyte solution. Hg/HgO electrode served as a reference electrode. Sintered $Ni(OH)_2$/NiOOH plate obtained from a commercial supplier was used as a counter electrode and got a much higher capacity as compared to the working electrode. The tests were performed using a LAND CT2001A Battery Tester. Before starting the tests, MH electrode was firstly activated for 10 cycles by fully charging it at a current density of 100 mA/g for 5 h and then discharged at 100 mA/g to the cut-off voltage of 0.7 V.

Alternating Current (AC) impedance measurements were

performed for both as cast and annealed alloys. SP-300-Potentiostat from Bio-Logic Science Instruments was used during the Electrochemical Impedance Spectroscopy (EIS) characterization. Galvanostatic Electrochemical Impedance Spectroscopy (GEIS) technique was applied in a range of frequencies from 1 kHz to 0.5 mHz when using the amplitude of the current of 10 mA. Four different States of Charge (SOC) of the electrodes were selected for the studies, including SOC 0% (completely discharged anode), 30, 70, and 100% (fully charged anode).

## 3. Results and discussion

### 3.1. Phase and structural composition

Figs. 1 and 2 show the XRD patterns of the

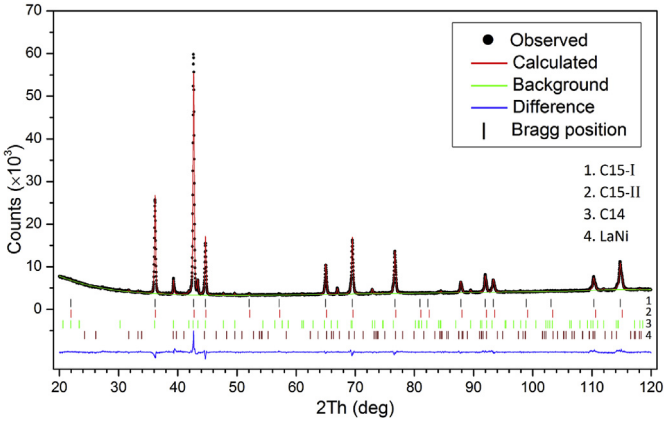


**Fig. 1.** XRD Rietveld refinements for the as cast alloy, $R_{wp} = 5.1\%$, $R_p = 3.8\%$, $\chi^2 = 3.5$.

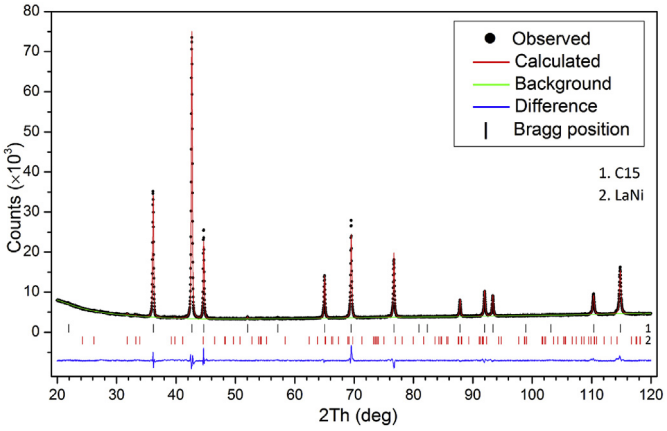


**Fig. 2.** XRD Rietveld refinements for the annealed alloy, $R_{wp} = 5.9\%$, $R_p = 4.2\%$, $\chi^2 = 4.3$.

$Ti_{0.15}Zr_{0.85}La_{0.03}Ni_{1.2}Mn_{0.7}V_{0.12}Fe_{0.12}$ as-cast and annealed alloys. Table 1 summarizes the crystallographic data, including refined unit cell parameters, unit cell volumes and phase abundances. Refinements show that as-cast alloy contains three Laves phases: C15–I (61.1 wt%) and C15–II (25.7 wt%) with FCC structures as the main phase, and C14 (12.1 wt%) intermetallic with hexagonal structure as a secondary phase. Furthermore, trace amounts of LaNi orthorhombic structure phase (the most intense peak 111 is clearly seen at 31.75°) were identified. The minor phases (except of LaNi) disappear during the annealing of the alloy at 950 °C (Table 1) and only one C15 intermetallic phase remains. Refinements of the XRD data show that the experimental and calculated pattern well agree with each other (Figs. 1 and 2).

Formation of three Laves phases are due to inhomogeneous distribution of the components in the alloy. Importantly, C15 phase is formed at higher Zr/Ti ratios while C14 intermetallic is formed at lower Zr/Ti ratios. A trend to form C14 phase increases with increasing Ti content. Increase of Ti content leads to a decrease in a lattice parameter of the C15 phase. Thus, Ti content in the C15–I phase should be smaller than that in the C15–II phase.

C14 phase was formed due to inhomogeneous distribution of the components in the as cast alloy. For the related $Zr_{1-x}Ti_xNi_{1.3}Mn_{0.7-y}V_y$ alloys with similar chemical composition, increase in Ti ($x > 0.2$) and vanadium ($y > 0.3$) contents leads to the formation of the C14 phase [31]. The C14 phase formation can be explained by a variation in Ti/Zr ratio between the multiphase components of the as cast alloy. Heat treatment results in a uniform distribution of the components and a formation of a pure C15 phase that is the most thermodynamically stable intermetallic for the given alloy composition.

Back-scattered electron SEM micrographs of the as-cast and annealed $Ti_{0.15}Zr_{0.85}La_{0.03}Ni_{1.2}Mn_{0.7}V_{0.12}Fe_{0.12}$ samples are presented in Fig. 3 and clearly show presence of two phases, a dark gray main phase together with light inclusions of a secondary phase. Table 2 shows the data of the elemental EDX analysis. According to the EDX analysis, the main (matrix) phase in the as-cast sample (1) is the $AB_2$ alloy while the secondary phase (2) is formed by lanthanum and nickel which are present in the atomic ratio La/Ni ≈ 1:1, with no contribution from the remaining elements. The content of the secondary phase is estimated as 3%. From quantitative analysis, the overall content of the elements well agrees with the gross formula of the alloy. In the annealed alloy, the fraction of the secondary phase significantly decreases, down to 1%. The reason for that could be in (a) Interaction of LaNi with metallurgical impurity of oxygen resulting in binding of O by La followed by a decrease of O content in the matrix phase; (b) Partial solubility of La in $AB_2$ matrix phase, probably at a trace level, but leading to a decrease on the content of LaNi secondary phase in the annealed alloy.

Even though the content of the secondary LaNi phase is rather low (1–3%) it was possible to identify it by XRD analysis. On the other hand, C14 Laves phase was also clearly identified by the XRD

**Table 1**
Crystallographic data for the $Ti_{0.15}Zr_{0.85}La_{0.03}Ni_{1.2}Mn_{0.7}V_{0.12}Fe_{0.12}$ as-cast and annealed alloys from Rietveld refinements of the XRD data.

| Sample | Phase | Space group | Unit cell parameters, Å | | | | Abundance, wt.% |
|---|---|---|---|---|---|---|---|
| | | | *a* | *b* | *c* | V, Å³ | |
| As-cast | C15–I | *Fd* $\bar{3}m$ | 7.0252(2) | – | – | 346.718(1) | 61.1(3) |
| | C15–II | *Fd* $\bar{3}m$ | 7.0125(3) | – | – | 344.841(2) | 25.7(2) |
| | C14 | $P6_3/mmc$ | 4.9813(3) | – | 8.1155(8) | 174.389(2) | 12.1(3) |
| | LaNi[a] | *Cmcm* | 3.906(6) | 10.77(2) | 4.399(7) | 185.055(4) | 1.1(1) |
| Annealed | C15 | *Fd* $\bar{3}m$ | 7.0235(1) | – | – | 346.466(1) | 99.1(1) |
| | LaNi | *Cmcm* | 3.902(7) | 10.78(2) | 4.385(8) | 184.449(6) | 0.9(1) |

[a] Rietveld refinements of LaNi phase were based on the reference data given in Ref. [33].

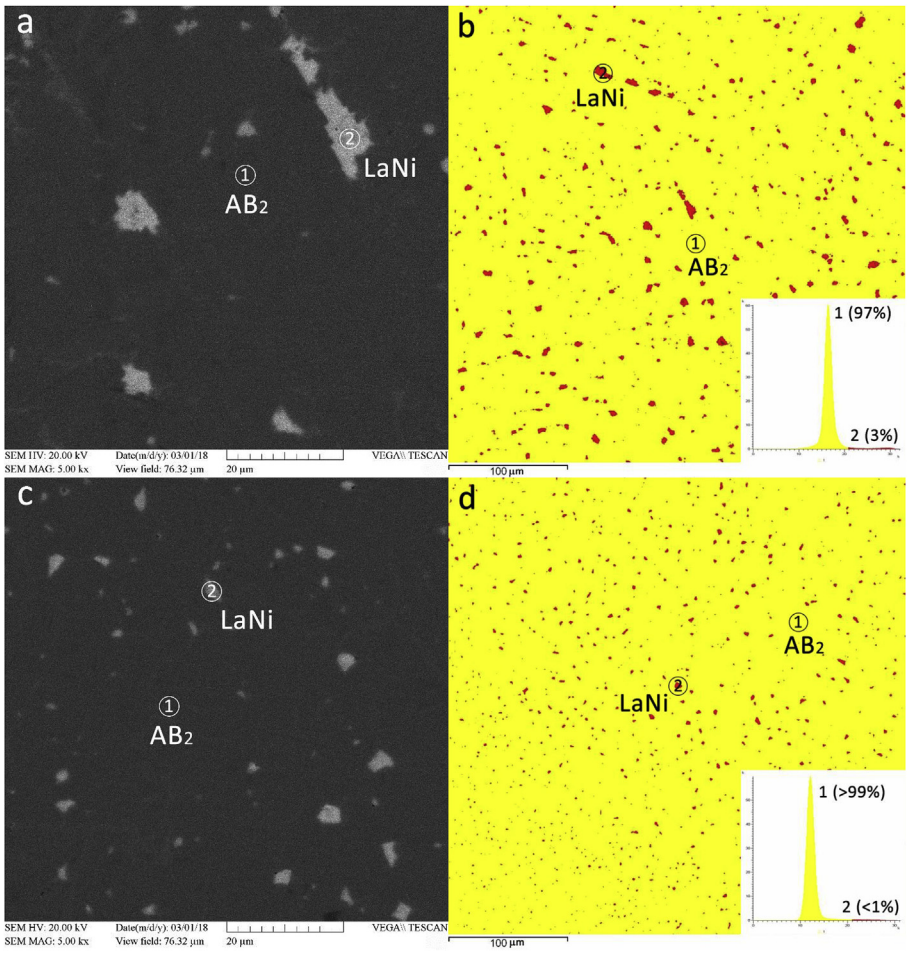


**Fig. 3.** SEM(BSE) (a,c) and EDX (b,d) images and abundances of the present phases, calculated from their areal in the $Ti_{0.15}Zr_{0.85}La_{0.03}Ni_{1.2}Mn_{0.7}V_{0.12}Fe_{0.12}$ as-cast (a and b) and annealed (c and d) alloys.

**Table 2**
Elemental compositions of $Ti_{0.15}Zr_{0.85}La_{0.03}Ni_{1.2}Mn_{0.7}V_{0.12}Fe_{0.12}$ (at.%) as cast and annealed at 950 °C alloys from EDX study.

| | Region | Ti | Zr | La | Ni | Mn | V | Fe |
|---|---|---|---|---|---|---|---|---|
| As cast alloy | 1 | 4.32 | 25.53 | 0.16 | 34.90 | 25.34 | 5.02 | 4.73 |
| | 2 | 0.15 | 0.33 | 48.54 | 48.58 | 1.43 | 0.97 | 0.00 |
| Annealed alloy | 1 | 5.50 | 26.55 | 0.17 | 37.45 | 21.95 | 4.45 | 3.93 |
| | 2 | 0.00 | 0.50 | 47.55 | 49.80 | 1.95 | 0.00 | 0.20 |
| | Std. Dev. | 0.60 | 0.20 | 0.12 | 0.45 | 0.40 | 0.25 | 0.20 |

study of the as cast alloy but was not distinguishable in the SEM micrographs due to an insignificant difference in its elemental composition in comparison with the main C15 phase.

From the reference publications it is known that La is poorly soluble in the Zr and Ti containing Laves phase MH alloys and thus it forms very limited solid solutions. Instead it forms a secondary LaNi phase, which is present in the microstructure as globular particles [34,35]. However, despite its very low content, the presence of the secondary LaNi phase is very important for the overall hydrogen storage performance. Indeed, LaNi absorbs a large amount of hydrogen during the initial activation forming $LaNiH_{3.6}$ [33] and contributes to an increase in the effective surface area due to the cracking and powdering of the alloy during the hydrogen absorption-desorption process. Thus, La acts as an initiator and promoter of the initial hydrogen absorption-desorption also improving the electrochemical performance at high current densities of charge and discharge.

### 3.2. Hydrogen absorption-desorption properties

Measured at room temperature isotherms of hydrogen absorption and desorption showed that maximum hydrogen storage capacity of the annealed $Ti_{0.15}Zr_{0.85}La_{0.03}Ni_{1.2}Mn_{0.7}V_{0.12}Fe_{0.12}$ alloy is 1.54 wt% H. At 293 K, equilibrium plateau of hydrogen desorption is close to 1 bar $H_2$ and shows presence of a broad and rather flat plateau (Fig. 4). It should be noted that the difference between the hydrogen absorption and desorption isotherms is rather small and the studied alloy shows a very small hysteresis. Hysteresis is an important intrinsic property of the alloy-hydrogen systems. From the PCT data, we conclude that hysteresis decreases with increasing temperature, indicating that the critical temperature in the studied system is low. Its evaluation from an intercept of the straight line dependances of lnP vs 1/T for absorption and desorption gives $T_{crit}$ value of around 393 K. The thermodynamic parameters of interaction – enthalpy (ΔH) and entropy (ΔS) changes – during the phase transformation - were obtained from the pressure-composition isotherms measured at different temperatures using the van't Hoff equation [25]:

$$ln(P_{H_2}) = \frac{\Delta H}{RT} - \frac{\Delta S}{R} \quad (1)$$

where $P_{H2}$ is equilibrium mid-plateau pressure in the PCT diagram and R is a universal gas constant. These values are equal to $\Delta H = -31 \pm 1$ (kJ/mol); $\Delta S = -110 \pm 5$ (J/K·mol) for the hydride

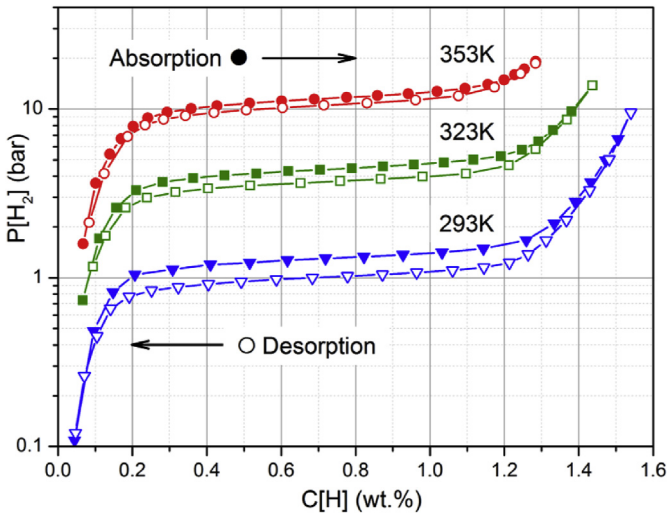


**Fig. 4.** PCT isotherms of hydrogen absorption-desorption for the annealed $Ti_{0.15}Zr_{0.85}La_{0.03}Ni_{1.2}Mn_{0.7}V_{0.12}Fe_{0.12}$ alloy.

formation process and $\Delta H = 34 \pm 1$ (kJ/mol); $\Delta S = 115 \pm 5$ (J/K·mol) for the hydride decomposition process (Fig. 5). Enthalpy change has a sufficiently low value, which allows a good reversibility of the system during the electrochemical charge and discharge of the battery anode when cycled in an open cell. The obtained values of ΔH and ΔS are in good agreement with the reference data for the chemically similar materials. As an example, in work [18] a similar value of $\Delta H = -33.7$ (kJ/mol) was obtained for the $Ti_{12}Zr_{21.5}V_{10}Cr_{7.5}Mn_{8.1}Co_8Ni_{32.2}Sn_{0.3}Al_{0.4}$ alloy based hydride.

Absorption/desorption hysteresis is a typical phenomenon observed in the metal-hydrogen systems. Hysteresis is related to the large volume expansion during a formation of the metal hydride, up to 25–30%. It causes stresses which appear during a growth of a hydride nucleus inside the alloy matrix having a smaller molar volume. The hysteresis decreases with increasing temperature. It should be noted that PCT plateau also become narrower with increasing temperature. Decreasing hysteresis can be explained by two factors: increased lattice mobility at a higher temperature and smaller volume change during a transition between the hydrogen solid solution and the hydride phase. Hysteresis completely disappears at critical temperature.

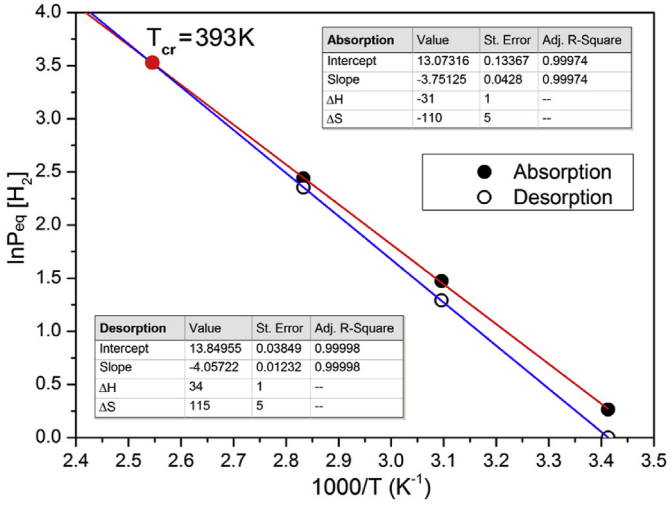


**Fig. 5.** Dependence between equilibrium pressure $\ln P_{eq}$ of hydrogen absorption and desorption and inverse temperature based on the PCT diagrams measured at 293, 323 and 353 K. Intersect of the straight lines for absorption and desorption gives a critical temperature $T_{crit}$ for the $Ti_{0.15}Zr_{0.85}La_{0.03}Ni_{1.2}Mn_{0.7}V_{0.12}Fe_{0.12}$-$H_2$ system of 393 K.

Critical temperature is the temperature above which a two-phase region, corresponding to the first order transition between α-H solid solution and β-hydride phase, is replaced by a second order transition with continuous changes in H content causing continuous changes in the unit cell parameters. Two-phase region appears as a pressure plateau in the PCT curve at a specific temperature; however, this plateau disappears above the critical temperature while the α-β transition becomes continuous. From the available data we conclude that $T_{crit}$ is rather low and equals to 393 K.

### 3.3. Hydrogen diffusion properties

Fig. 6 and Table 3 present the data describing a relationship between the hydrogen diffusion coefficient and state of charge (SOC) for the annealed $Ti_{0.15}Zr_{0.85}La_{0.03}Ni_{1.2}Mn_{0.7}V_{0.12}Fe_{0.12}$ alloy electrode. The measurements were carried out by potentiostatic intermittent titration technique (PITT) at low amplitude (0.02 V) current transients in the potentials range from −0.80 to −0.96 V (Fig. 6a). To calculate the effective hydrogen diffusion coefficient, we used $It^{1/2}$ vs. log t plots allowing to locate a «Cottrellian maximum» and to find the corresponding time range needed to perform the calculations. The observed maximum demonstrates pronounced deviations from a steady-state planar diffusion, as well as presence of non-diffusion type slow processes in certain time domains (including effect of Ohmic potential drop in the solution at high currents). The region of a pit in Fig. 6b is the «most Cotrellian » part of the transients. Then $1/It^{1/2}$ vs. $1/t^{1/2}$ plots were used to account for the deviations from the ideal Cottrellian dependence caused by the Ohmic losses, and to calculate D (Fig. 6c). Hydrogen diffusion coefficient was calculated according to a modified Cottrell Equation (see Refs. [36,37] for the details):

$$\frac{1}{I\sqrt{t}} = \frac{R_{\sum}}{\Delta E\sqrt{t}} + \frac{l\sqrt{\pi}}{\Delta Q\sqrt{D}} \quad (2)$$

where $R_{\Sigma} = R_{solution} + ; R_{surface\ films} + R_{charge\ transfer}$; $\Delta Q$ is the total charge of electrode at a certain potential; $l$ is diffusion length that is equal to a half of a metal particle size ($2.5 \times 10^{-3}$ cm).

The obtained plots corresponding to Eq. (2) and the calculated D values are shown in Fig. 6d and in Table 3. Total resistance $R_{\Sigma}$ determined from the slope of this plot equals to 2.6 Ohm. We also estimated $R_{solution} + R_{surface\ films}$ (RR) contribution independently, by interrupting polarization during the galvanostatic measurements. A sharp decrease of the potential after this interruption corresponded to 0.24 Ohm, which is by one order of magnitude smaller than RR. Even though analysis of all separate contributions is beyond the scope of this paper, we underline that the resistance caused by the charge transfer is an essential part of the overall $R_{\Sigma}$ and cannot be ignored. However, for the studied experiment RR had a small value, and the deviations from Cottrell behavior were not significant. The maximum value of D ($2.84 \times 10^{-9}$ cm$^2$/s) was obtained at a minimum studied state of charge (SOC) of 2.1%. Hereinafter as the state of the charge increased, hydrogen diffusion coefficient became lower decreasing to $4.55 \times 10^{-13}$ cm$^2$/s. Such a behavior is typical for all hydride-forming alloys [35]. Nevertheless, the obtained maximal values of D are somewhat higher as compared with the $AB_3$ based hydrides (for example, $2.87 \times 10^{-11}$ cm$^2$/s for $La_{1.5}Nd_{0.5}MgNi_9$) [37] and $AB_5$ based hydrides ($1.81 \times 10^{-10}$ cm$^2$/s for $MmNi_{4.25}Mn_{0.25}Co_{0.45}Al_{0.3}$) [38] type alloys.

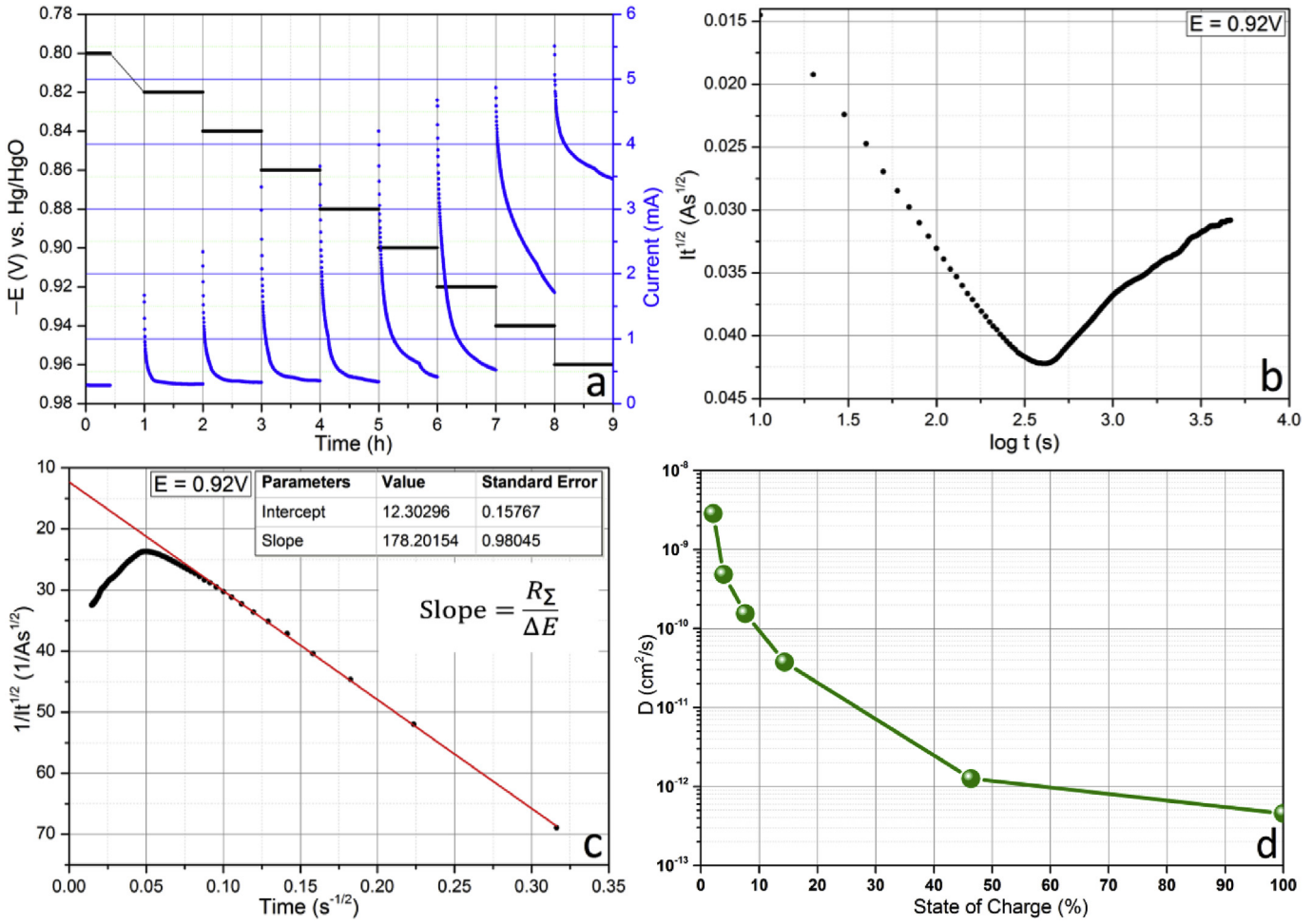


**Fig. 6.** Time dependence of the currents as related to the applied potential (a); «Cottrellian maximum» from graph plotted in $It^{1/2}$ vs. log t coordinates for E = −0.92 V (b); Linear fitting analysis derived from graph plotted in $1/It^{1/2}$ vs. $1/t^{1/2}$ coordinates for E = −0.92 V (c); The dependence of the effective hydrogen diffusion coefficient on the state of charge of the electrode (d).

### 3.4. Electrochemical properties

Lanthanum present in the alloy caused the formation of a La-rich LaNi intermetallic compound which efficiently catalyzed the process of activation of the electrodes. Both as-cast and annealed alloys approached maximum capacity during the fourth charge-discharge cycles and then showed only a slight increase in the capacities (Fig. 7). The maximum capacity during the activation of the cast alloy at a charge-discharge current density of 100 mA/g was 345 mAh/g, while for the annealed alloy it was higher reaching 370 mAh/g.

Similar studies were performed in Ref. [28] where the activation behavior of an $AB_2$-type $(Ti_{0.36}Zr_{0.64})(V_{0.15}Ni_{0.58}Mn_{0.20}Cr_{0.07})_2$ Laves phase alloy was investigated and lanthanum was not present in the alloy. The alloy contained C14 Laves phase as the main constituent and $(Ti_{0.5}Zr_{0.5})Ni$ intermetallic as a secondary phase. Untreated alloy initially had almost zero capacity and reached a capacity of

**Table 3**
Diffusion parameters as related to the state of charge for the annealed $Ti_{0.15}Zr_{0.85}La_{0.03}Ni_{1.2}Mn_{0.7}V_{0.12}Fe_{0.12}$ alloy electrode at different potentials.

| Potential, V | Capacity, mAh | SOC % | $1/It^{1/2}$ | Slope | D, $cm^2/s$ |
|---|---|---|---|---|---|
| −0.80 | 0.02 | 0.1 | – | – | – |
| −0.82 | 0.08 | 0.6 | – | – | – |
| −0.84 | 0.11 | 1.2 | – | – | – |
| −0.86 | 0.17 | 2.1 | 47.45 | 183.25 | $2.84 \times 10^{-09}$ |
| −0.88 | 0.32 | 3.9 | 28.23 | 203.58 | $4.81 \times 10^{-10}$ |
| −0.90 | 0.67 | 7.6 | 22.33 | 170.34 | $1.54 \times 10^{-10}$ |
| −0.92 | 1.21 | 14.4 | 12.30 | 178.20 | $3.76 \times 10^{-11}$ |
| −0.94 | 5.74 | 46.4 | 4.84 | 196.06 | $1.26 \times 10^{-12}$ |
| −0.96 | 9.63 | 100 | 2.03 | 191.48 | $4.55 \times 10^{-13}$ |

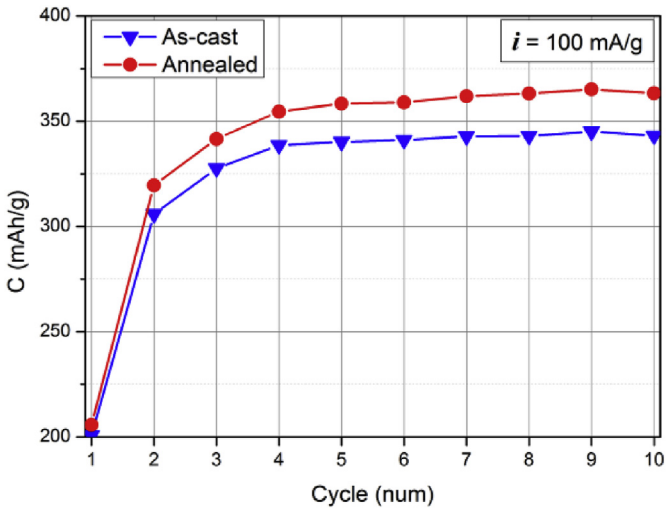


**Fig. 7.** Activation performance of the as-cast and annealed $Ti_{0.15}Zr_{0.85}La_{0.03}Ni_{1.2}Mn_{0.7}V_{0.12}Fe_{0.12}$ alloy electrodes.

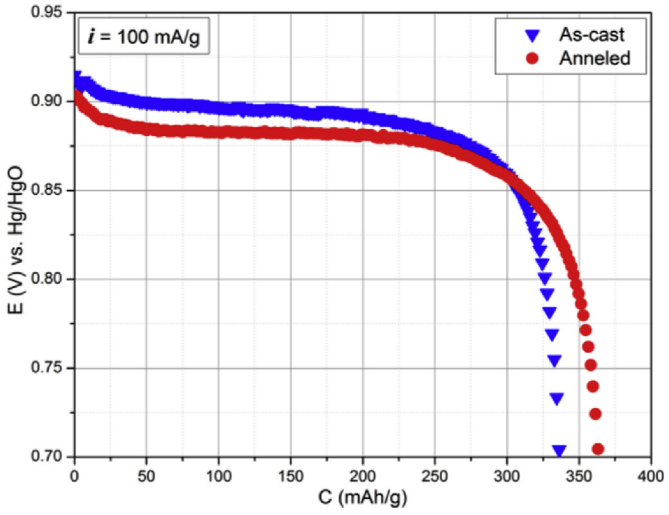


**Fig. 8.** Discharge capacity of the as-cast and annealed $Ti_{0.15}Zr_{0.85}La_{0.03}Ni_{1.2}Mn_{0.7}V_{0.12}Fe_{0.12}$ alloy electrodes.

220 mAh/g only after 14 cycles. A significant improvement of the activation performance of the alloy was achieved only after boiling of the alloy powder in a hot KOH solution for 80 min. After that it was possible to achieve a capacity of 390 mAh/g. In contrast, the alloys containing lanthanum which were used in Refs. [10,13], reached maximum capacity values already at the very beginning of the activation without any additional processing. In all cases, the presence of a secondary La-Ni phase was noted. From that we conclude that presence of La in the composition of the alloy is essential to reach its efficient activation performance.

It should be noted that in addition to the larger discharge capacity, the annealed alloy had a flatter and broader plateau of discharge potentials which is located between −0.85 and −0.9 V (Fig. 8). Furthermore, the plateau of potential for the annealed alloy moves to the slightly less negative values (middle of the plateau is located at −0.88 V) as compared to as-cast alloy (middle of the plateau at −0.90 V) which corresponds to a lower pressure of desorption of hydrogen from the metal hydride formed by the annealed alloy. Furthermore, the annealed alloy shows a better high rate dischargeability and a higher cyclic stability as compared to the as-cast alloy. The discharge capacity reaches 65% (246 mAh/g) at a discharge current density of 1000 mA/g (Fig. 9a and b). After 100 cycles with 100% DOD at discharge current density of 300 mA/g (1C), the discharge capacity for the annealed alloy equaled to 90% of the initial capacity which is 10% higher as compared to the as-cast alloy (Fig. 10). Improved performance of the annealed alloy appears to be related to its more homogeneous composition resulting from the annealing process.

The improvement of HRD performance after the annealing well correlates with increased hydrogen diffusion coefficient in the annealed alloy as compared to that of the as-cast alloy. Such improvements can be related to the changes in the structure as the annealed alloy contains only C15 intermetallic and this phase is known to be superior for the high-power batteries and is superior to the hexagonal C14 alloy which transforms into a homogeneous C15 type alloy after the annealing. Furthermore, the microstructure of the alloy changes after the annealing treatment. As can be seen from the micrographs (Fig. 3), after the annealing LaNi phase becomes uniformly and finely dispersed in the alloy matrix and shows presence of very small particles. The amount of LaNi visibly decreases based on the area occupied by LaNi in the SEM image but also decreases, even though less significantly, based on the analysis

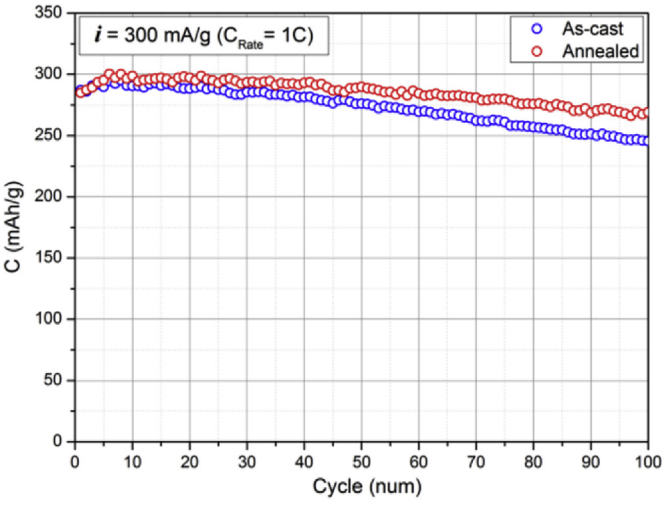


**Fig. 10.** Cyclic stability of the as-cast and annealed $Ti_{0.15}Zr_{0.85}La_{0.03}Ni_{1.2}Mn_{0.7}V_{0.12}Fe_{0.12}$ alloy electrodes.

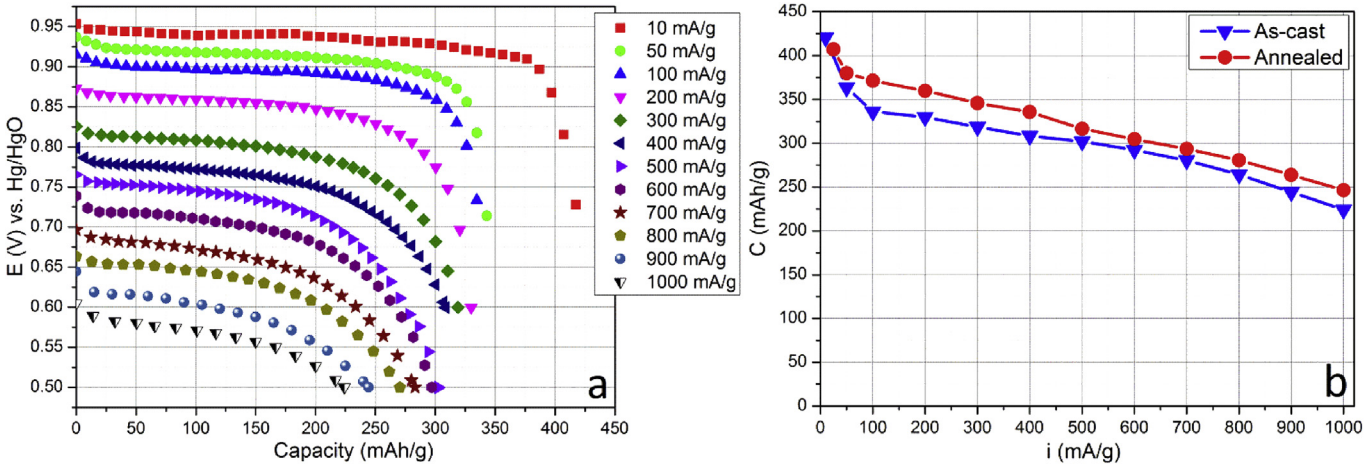


**Fig. 9.** The capacity of the as-cast $Ti_{0.15}Zr_{0.85}La_{0.03}Ni_{1.2}Mn_{0.7}V_{0.12}Fe_{0.12}$ alloy electrode at different current densities and cut-off potentials (a); High-rate dischargeability of the as-cast and annealed alloy electrodes (b).

of the XRD data. This could be associated with the fact that La from LaNi can raffinate the alloy from the metallurgical oxygen thus purifying the grain boundaries by removing the Ti/Zr-containing oxides because of the formation of the clusters of $La_2O_3$. Because of that the activity of these alloys in the hydrogenation process becomes higher. Finally, the reason for such a change could be in partial solubility of La in $AB_2$ matrix phase, probably at a trace level, leading to a decrease of LaNi content in the alloy.

The annealing treatment leads to the homogenization of the alloy composition and formation of a pure C15 Laves phase intermetallic. This results in a higher reversible H storage capacity of the alloy. In addition, LaNi phase (which acts as a catalyst of hydrogen absorption) becomes finely and uniformly dispersed in the alloy. This results in an increased hydrogen diffusion coefficient and improved high rate dischargeability of the annealed alloy. An improvement in the electrochemical characteristics after the annealing was observed by us earlier when studying $AB_3$ and $A_2B_7$ type alloys, and the values of specific capacitance, HRD, and cyclic stability obtained in this study are quite comparable with the data for the La-Mg-Ni alloys [39–44]. Further studies of the effect of the rare earth metals on the improved electrochemical performance of the Zr-based Laves type alloys are required to better understand the mechanism governing catalytic interaction between the main phase and the rare earth containing secondary phases, to systematically extend observations available for the multiphase Zr-based alloys doped by La, Ce, Pr or Nd [45] or Zr-based C15 type Laves phase alloys doped by 3 wt% La [46].

### 3.5. Electrochemical Impedance Spectroscopy (EIS) characterization

Electrochemical impedance spectroscopy (EIS) was applied to characterize the kinetics of surface electrochemical reactions occurring in the studied electrode [47]. This technique is very sensitive and is very useful; however, it meets the challenges in the evaluation of the data due to a multiparameter dependence of the results from the various processes taking place in the studied samples. The objective of the current study was in evaluating how State of Charge and homogeneity of the samples affects their impedance/resistivity and rates of hydrogen diffusion in the electrode.

The most commonly used to model the Nyquist impedance dependencies contain a hemicycle and a straight-line part which can be modeled by a Randles equivalent circuit consisting of a charge transfer resistance ($R_{ct}$) connected in series with a Warburg impedance ($Z_w$) and in parallel with a double-layer capacitance ($C_{dl}$) (Fig. 11a). It appears that the original Randles circuit is not suitable to fit the experimentally measured in present work Nyquist plot because of a more complex shape of the latter plot indicating that several processes are contributing to the collected data. To fit a more complex experimentally measured data than described by a classical Nyquist plot (Fig. 11b), Randles equivalent circuit has been modified by including a Constant Phase Element (CPE), which is connected in parallel while the individual Warburg impedance is in a series connection. Capacitance was replaced by CPE to describe the depressed hemicycle shape of the Nyquist plot which can originate from the surface inhomogeneity of the electrodes. A CPE is introduced because the semicircles in the Nyquist plots are depressed due to heterogeneity of the surface/surface roughness, or other effects that cause uneven current distributions at the electrode surface [48]. By replacing the capacitance C with CPE in the equivalent circuit, a much better fit of the EIS was achieved. Furthermore, in the present study, an additional parallel circuit element consisting of R and CPE in series was added to achieve a more accurate modeling of the studied electrode.

The circuit element capacitance, C, has an impedance of:

$$Z_C = \frac{1}{j\omega C} \tag{3}$$

while the impedance for CPE is:

$$Z_{CPE} = \frac{1}{Y_0(j\omega)^n} \tag{4}$$

where, $Y_0$ is the admittance of an ideal capacitance and $n$ is an empirical constant, ranging from 0 to 1. We note that when $n = 1$, the CPE behaves as a pure capacitor $C = Y_0$, while when $n = 0$, the CPE behaves a pure resistor $R = Y_0^{-1}$. Furthermore, when $n = 0.5$, the CPE is an equivalent of the Warburg element.

To fit the Nyquist impedance, the observed impedance dependence was assumed to consist of two individual hemicycles as shown in Fig. 12. These two hemicycles are related to the selected circuits as depicted in the lower part of Fig. 12. The first arc in the higher frequency range represents the electrolyte resistance shown by intersection of the smallest arc with the real axis of impedance ($Z_{real}$), and the contact resistance and capacitance between the

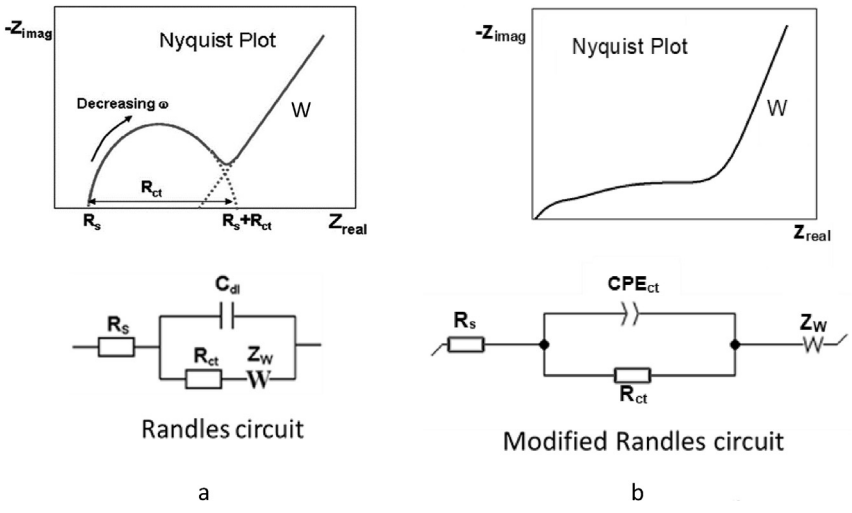


**Fig. 11.** Original (a) and modified (b) of Nyquist plots containing charge transfer resistance and Warburg element (W).

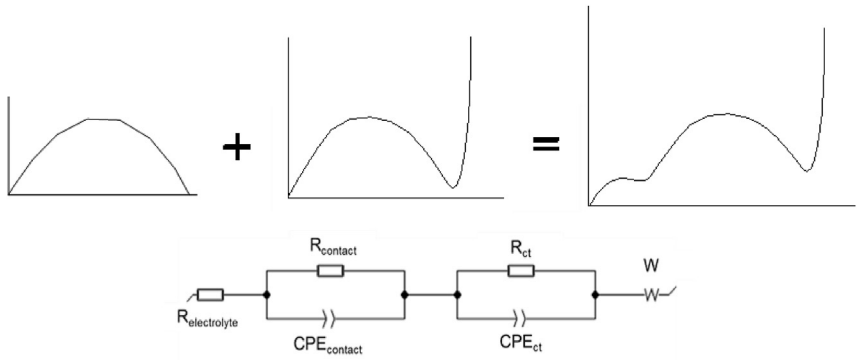


**Fig. 12.** Equivalent circuit well describing the Nyquist impedance plot.

current collector and the alloy particles ($R_{contact}$), while the second arc is related to the charge transfer resistance ($R_{ct}$) and the capacitance of the electrode surface containing the Warburg element (W).

Following the circuits model described above, the EIS experimental data for each studied sample was fitted and deconvoluted to determine the values of individual circuit components. The deconvolution has been done by setting two initial semicircles and a linear part to represent the assumed circuit model. Typical deconvolution procedure results in obtaining EIS parameters for the individual deconvoluted parts which overlap with each other resulting in the overall EIS shown in Fig. 13.

From the fitting process on the EC-Lab, 8 different parameters describing the properties of the studied system were obtained, including $R_{electrolyte}$, $R_{contact}$, $CPE_{contact}$, $n_1$, $R_{charge\ transfer}$, $CPE_{charge\ transfer}$, $n_2$, and σ. The fitting values of these parameters for as-cast and annealed alloys are shown in Table 4, while the plots presenting experimental data and modeling results as related to the SOC of the anodes are given in Supplementary Information, Fig. S1 (for as cast alloy) and Fig. S2 (annealed alloy). Excellent fit of the experimental data has been achieved by using such modeling. Quality of the fit can be evaluated by calculating the Goodness of fit ($\chi^2$) values and Coefficient of determination ($R^2$).

When comparing the data of numerical fitting, we can easily conclude that fitting of two hemispherical parts shows their very

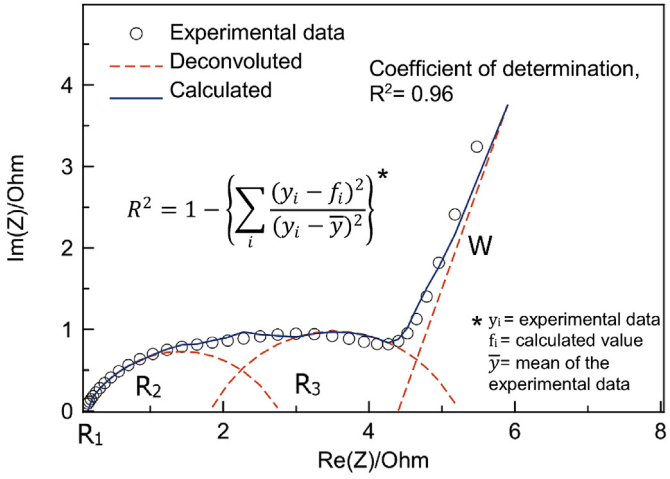


**Fig. 13.** Deconvolution of Nyquist impedance plot for 0% SOC of as cast alloy achieved by using a superposition of equivalent circuits, where $R_1 = R_{electrolyte}$, $R_2 = R_{contact}$, $R_3 = R_{ct}$, and W = Warburg element. As the value of R2 is rather close to 1, this shows that the proposed fit well described the data.

different properties. By applying annealing of the alloy, almost all parameters including electrolyte resistance, contact resistance, and Warburg element decreased, showing that the annealing generally reduces the total resistance. Furthermore, the hydrogen transport in the annealed alloy is faster than in the as-cast alloy. In addition, the fitted value of CPE for contact and charge transfer impedance and the empirical constant for CPE for the as-cast alloy are larger than for the annealed alloy. The reason for that is in a fact that the annealing improves the homogeneity of the alloy and enlarges the surface area of the alloy. We note that increasing of $R_{ct}$ for some SOC due to the annealing process gives a smaller effect on hydrogen diffusion as compared to the decrease of the value of the Warburg element. This happens because H diffusion coefficient is proportional to an inverse square of Warburg element, as it follows from a simplified equation of Fick's diffusion in a metal hydride.

The following equation has been utilized to determine the diffusion coefficient $D_H$ [49]:

$$D_H = \frac{R^2T^2}{2A^2n^4F^4C^2\sigma^2} \quad (5)$$

where $D_H$ – diffusion coefficient of hydrogen; R – ideal gas constant; T – absolute temperature; A – electroactive surface area per unit volume of electrode; n – number of electrons transferred; C – concentration of hydrogen ions; σ – Warburg impedance coefficient.

The electroactive surface area, A, was estimated assuming that the spherical alloy particles in the studied electrode all have the same size and their entire surface is exposed to the electrolyte, being described by the following expression [50]:

$$A = \frac{3(1-\in)}{r} \quad (6)$$

where ∈ = electrode porosity, assumed to be 0.3 [51]; r = radius of spherical particle (active alloy), an average value was chosen as 25 μm (as mentioned in the experimental part).

From the fitting results, it is easy to conclude that annealing increases the rate of hydrogen diffusion as compared to the as-cast alloy. In line with these observations, the fitting of the EIS data showed differences appearing between the as cast and annealed samples. In particular, it could be noted that the annealed alloy shows a smaller Nyquist impedance resistance as compared to the as cast one. This could be related to the increased homogeneity of the annealed alloy which contains 99.4 wt% of the C15 phase. For the as cast alloy content of C15 phase was smaller, 94.5 wt%.

As expected, impedance spectrum is strongly dependent upon state of charge of the electrodes. The refined values of the hydrogen diffusion coefficient are significantly lower for the samples of the

**Table 4**
Fitted parameters of EIS spectra for the as-cast and annealed $Ti_{0.15}Zr_{0.85}La_{0.03}Ni_{1.2}Mn_{0.7}V_{0.12}Fe_{0.12}$ alloy.

| Parameters | 0% SOC | | 30% SOC | | 70% SOC | | 100% SOC | |
|---|---|---|---|---|---|---|---|---|
| | As-cast | Annealed | As-cast | Annealed | As-cast | Annealed | As-cast | Annealed |
| $R_{electrolyte}$, Ohm | 0.1247 | 0.08927 | 0.1350 | 0.07515 | 0.1360 | 0.06093 | 0.1574 | 0.07609 |
| $R_{contact}$, Ohm | 2.1670 | 1.306 | 1.8570 | 1.812 | 2.133 | 1.128 | 2.3660 | 1.964 |
| $CPE_{contact}$, $F.s^{\alpha-1}$ | 0.5213 | 0.6748 | 0.3652 | 0.3129 | 0.2648 | 0.456 | 0.2880 | 0.3152 |
| $n_1$ | 0.7592 | 0.905 | 0.9039 | 0.8893 | 0.7858 | 0.9918 | 0.7864 | 0.7532 |
| $R_{ct}$, Ohm | 1.9990 | 2.219 | 3.054 | 2.686 | 2.751 | 2.987 | 2.730 | 2.331 |
| $CPE_{ct}$, $F.s^{\alpha-1}$ | 0.05219 | 0.05697 | 0.03525 | 0.04039 | 0.03679 | 0.04328 | 0.03559 | 0.04313 |
| $n_2$ | 0.6459 | 0.6569 | 0.6750 | 0.6741 | 0.662 | 0.6647 | 0.6781 | 0.6662 |
| σ, $Ohm.s^{1/2}$ | 0.2366 | 0.2040 | 0.02547 | 0.02199 | 0.02727 | 0.0250 | 0.02802 | 0.02700 |
| Goodness of fit, $\chi^2$[a] | 0.05429 | 0.1855 | 0.07281 | 0.1159 | 0.09871 | 0.3070 | 0.04163 | 0.1610 |
| $D_H$, $cm^2.s^{-1}$ | $3.59e^{-12}$ | $4.82e^{-12}$ | $3.09e^{-10}$ | $4.15e^{-10}$ | $2.70e^{-10}$ | $3.21e^{-10}$ | $2.56e^{-10}$ | $2.75e^{-10}$ |

[a] $\chi^2 = \sum_{i=1}^{n} \frac{|Z_{meas}(i) - Z_{model}(f_i, param)|^2}{\sigma_i^2}$

where,
$Z_{meas}$ (i) = measured impedance at $f_i$ frequency
$Z_{model}$ (fi, param) = calculated impedance, based on a selected model
$f_i$ = frequency
param = model parameters (R1, R2, C1, Q1)
$\sigma_i$ = standard deviation

initial intermetallic alloy with 0% SOC, both for the as-cast and the annealed alloy. With further saturation of the alloy by hydrogen when a transformation from α-solid solution to the β-hydride phase takes place, the hydrogen diffusion in bulk of the alloy increases sharply and then decreases as extent of the alloy's transformation into the hydride progresses from 30 to 100% SOC (Fig. 14).

From the data collected at different SOC, it can be clearly seen that annealed alloy has lower contact resistances and lower Warburg element values as compared to the as cast alloy. The annealing improves the homogeneity of the phase structure where C15 is the dominant phase, which results in a to decreased resistance between the alloys particles and between the alloy and the current collector. However, a larger total area of the C15 phase contributes to the larger $CPE_{ct}$ values and makes the charge transfer process becoming more difficult to accomplish, therefore the $R_{ct}$ should be higher in the annealed alloy in comparison with that for the as cast alloy.

When comparing the data of the PITT and EIS experiments, we should stress that investigating the hydrogen diffusion using PITT measurements neglects the interfacial resistance and assumes that the system is diffusion-controlled. This can result in smaller $D_H$ values than these values when using the EIS technique [52]. The diffusion coefficient derived from PITT measurements is calculated based on Cottrell equation, which is directly related to the time and concentration of the species undergoing a transient diffusion. The Ohmic potential drops, interfacial kinetics, double-layer charging and phase transitions in the bulk of host materials are neglected in this approach. This is very much different from the EIS techniques, where the diffusion process is assessed for a steady state diffusion mode. Furthermore, in the real conditions, the diffusion is the rate limiting step of the mass transport being independent of time. In the Cottrell domain, there are two diffusion control paths, a semi-infinite diffusion in a short-time domain and the finite-space diffusion in a long-time domain [53]. The semi-infinite diffusion in the short-time domain was considered during evaluation of the EIS data to obtain the diffusion coefficient of hydrogen, which is thus very much dependent of the time-dependent changes of hydrogen concentration during the short-time diffusion.

To conclude, none of the above methods (PITT and EIS) gives an unambiguous absolute value of the diffusion coefficient of hydrogen and can be used for a rough estimation of the $D_H$ only. Nevertheless, the data obtained by using these two methods well correlate with each other, and the obtained values of $D_H$ are mutually consistent and well agree with the reference data.

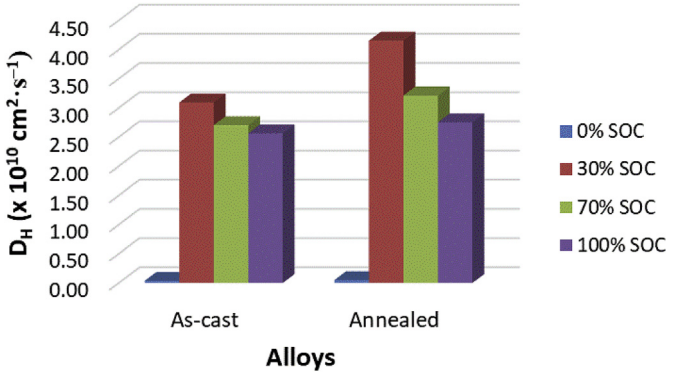


**Fig. 14.** Hydrogen diffusion coefficient for the as-cast and annealed alloys as related to SOC of the electrodes. The blue bars in Fig. 14 show the smallest values of hydrogen diffusion coefficient observed at 0% SOC. (For interpretation of the references to colour in this figure legend, the reader is referred to the Web version of this article.)

## 4. Conclusions

The $AB_2$-type $Ti_{0.15}Zr_{0.85}La_{0.03}Ni_{1.2}Mn_{0.7}V_{0.12}Fe_{0.12}$ alloy was prepared by arc melting and annealing. Rietveld refinements of the XRD data show that the as-cast alloy contains three Laves phases: FCC C15–I (61.1 wt%) and C15–II (25.7 wt%) intermetallics as the main component, and C14 (12.1 wt%) type hexagonal alloy as a secondary phase, together with trace amounts (appr. 1 wt%) of orthorhombic LaNi intermetallic which was however clearly identified in the XRD and SEM data. The homogenization by annealing at 950 °C results in disappearance of the secondary C14 phase (while the amount of LaNi slightly decreases).

At room temperature, the annealed alloy has a low, close to 1 bar $H_2$ ($\Delta H_{des} = 34 \pm 1$ (kJ/mol); $\Delta S_{des} = 115 \pm 5$ (J/K·mol); critical temperature 393 K), plateau of hydrogen absorption-desorption and shows a very small hysteresis, flat equilibrium plateaux and H storage capacity of 1.54 wt% H.

Both as-cast and annealed alloys reach maximum H storage capacity already in the fourth activation cycle. The maximum

capacity is higher for the annealed alloy reaching 370 mAh/g (345 mAh/g for the as cast material). The annealed alloy shows higher values of HRD capacity and a better cyclic stability as compared to the as-cast alloy. After 100 cycles with 100% DOD at discharge current density of 300 mA/g (1C), the discharge capacity for annealed alloy amounted 90% of the initial capacity.

The phase-structural composition affects the EIS behavior and the alloy with the highest content of C15 Laves phase present in the annealed alloy shows the fastest hydrogen diffusion. SOC of the electrode has a direct influence on the rates of hydrogen diffusion which reaches maximum values for the electrodes with smallest SOC of 2%.

The electrochemical behavior of the alloy is significantly affected by the secondary LaNi phase which acts as a catalyst of hydrogen sorption-desorption processes, both during the alloy-$H_2$ gas interactions and during the electrochemical tests in aqueous electrolyte.

## Acknowledgements

This work was supported by the Norwegian Research Council (project “High Power Batteries Probed by Neutron Scattering”, program SYNKNØYT; RCN project 234246), IEA Task 32 project Hydrogen Based Energy Storage (RCN project 285146) and Norwegian Research Center on Zero Emission Energy Systems for Transport – FME MoZEES.

Alexei A. Volodin acknowledges the support from the Russian Science Foundation (PRJ No. 17-79-20413).

C.B. Wan acknowledges the support from the China National Natural Science Foundation (Grant No. 11605007).

Boris P. Tarasov acknowledges support from the Ministry of Science and Higher Education at the studies metal hydride materials microstructures (PRJ UI RFMEFI61318X0087).

## Appendix A. Supplementary data

Supplementary data to this article can be found online at https://doi.org/10.1016/j.jallcom.2019.03.134.

## References

[1] K. Young, J. Nei, The current status of hydrogen storage alloy development for electrochemical applications, Materials 6 (2013) 4574.
[2] K. Young, J. Nei, C. Wan, R.V. Denys, V.A. Yartys, Comparison of C14-and C15-predomiated $AB_2$ metal hydride alloys for electrochemical applications, Batteries 3 (2017) 22.
[3] K. Young, J.M. Koch, C. Wan, R.V. Denys, V.A. Yartys, Cell performance comparison between C14-and C15-predomiated $AB_2$ metal hydride alloys, Batteries 3 (2017) 29.
[4] K. Young, T. Ouchi, J. Koch, M.A. Fetcenko, Compositional optimization of V-free hypo-stoichiometric $AB_2$ metal hydride alloy for Ni/MH battery application, J. Alloys Compd. 510 (2012) 97–106.
[5] Y. Zhang, J. Li, T. Zhang, T. Wu, H. Kou, X. Xue, Hydrogenation thermokinetics and activation behavior of non-stoichiometric Zr-based Laves alloys with enhanced hydrogen storage capacity, J. Alloys Compd. 694 (2017) 300–308.
[6] M. Tliha, C. Khaldi, S. Boussami, N. Fenineche, O. El-Kedim, H. Mathlouthi, J. Lamloumi, Kinetic and thermodynamic studies of hydrogen storage alloys as negative electrode materials for Ni/MH batteries: a review, J. Solid State Electrochem. 18 (2014) 577–593.
[7] Y. Zhang, J. Li, T. Zhang, H. Kou, R. Hu, X. Xue, Hydrogen storage properties of non-stoichiometric $Zr_{0.9}Ti_xV_2$ melt-spun ribbons, Energy 114 (2016) 1147–1154.
[8] A. Matsuyama, H. Mizutani, T. Kozuka, H. Inoue, Effect of Ti substitution on electrochemical properties of ZrNi alloy electrode for use in nickel-metal hydride batteries, Int. J. Hydrogen Energy 42 (2017) 22622–22627.
[9] L. Kong, X. Li, K. Young, J. Nei, X. Liao, W. Li, Effects of rare-earth element additions to Laves phase-related body-centered-cubic solid solution metal hydride alloys: thermodynamic and electrochemical properties, J. Alloys Compd. 737 (2018) 174–183.
[10] Y. Zhang, W. Zhang, Z. Yuan, H. Shang, Y. Li, S. Guo, Structures and electrochemical hydrogen storage properties of melt-spun RE-Mg–Ni–Co–Al alloys, Int. J. Hydrogen Energy 42 (2017) 14227–14245.
[11] Y. Zhang, S. Cui, Y. Li, H. Shang, Y. Qi, D. Zhao, Structures and electrochemical performances of as-spun RE-Mg-Ni-Co-Al alloys applied to Ni-MH battery, J. Mater. Sci. Technol. 34 (2018) 370–378.
[12] S. Yasuoka, J. Ishida, K. Kishida, H. Inui, Effects of cerium on the hydrogen absorption-desorption properties of rare earth-Mg-Ni hydrogen-absorbing alloys, J. Power Sources 346 (2017) 56–62.
[13] T. Zhai, T. Yang, Z. Yuan, Y. Zhang, An investigation on electrochemical and gaseous hydrogen storage performances of as-cast $La_{1-x}Pr_xMgNi_{3.6}Co_{0.4}$ (x=0–0.4) alloys, Int. J. Hydrogen Energy 39 (2014) 14282–14287.
[14] D.F. Wong, K. Young, J. Nei, L. Wang, K.Y.S. Ng, Effects of Nd-addition on the structural, hydrogen storage, and electrochemical properties of C14 metal hydride alloys, J. Alloys Compd. 647 (2015) 507–518.
[15] K. Young, T. Ouchi, J. Nei, T. Meng, Effects of Cr, Zr, V, Mn, Fe, and Co to the hydride properties of Laves phase-related body-centered-cubic solid solution alloys, J. Power Sources 281 (2015) 164–172.
[16] E. Teliz, J. Diez, R. Faccio, F. Ruiz, F. Zinola, V. Díaz, Molybdenum incorporation on $AB_2$ alloys-part I metallurgical and electrochemical characterization: electrocatalytic behavior, J. Alloys Compd. 744 (2018) 583–590.
[17] E. Teliz, J. Diez, R. Faccio, E. German, F. Zinola, V. Díaz, Molybdenum incorporation on $AB_2$ alloys-Part II. On the synergetic effects of Laves and non-Laves phases, J. Alloys Compd. 737 (2018) 530–535.
[18] K. Young, T. Ouchi, X. Lin, B. Reichman, Effects of Zn-addition to C14 metal hydride alloys and comparisons to Si, Fe, Cu, Y, and Mo-additives, J. Alloys Compd. 655 (2016) 50–59.
[19] Z. Li, H. Wang, L. Ouyang, J. Liu, M. Zhu, Reversible hydriding in $YFe_{2-x}Al_x$ (x= 0.3, 0.5, 0.7) intermetallic compounds, J. Alloys Compd. 689 (2016) 843–848.
[20] K. Young, B. Chao, L. Bendersky, K. Wang, $Ti_{12.5}Zr_{21}V_{10}Cr_{8.5}Mn_xCo_{1.5}Ni_{46.5-x}$ $AB_2$-type metal hydride alloys for electrochemical storage application: Part 2. Hydrogen storage and electrochemical properties, J. Power Sources 218 (2012) 487–494.
[21] K. Young, D. Wong, S. Yasuoka, J. Ishida, J. Nei, J. Koch, Different failure modes for V-containing and V-free $AB_2$ metal hydride alloys, J. Power Sources 251 (2014) 170–177.
[22] S. Khajavi, M. Rajabi, J. Huot, Crystal structure of as-cast and heat-treated $Ti_{0.5}Zr_{0.5}(Mn_{1-x}Fe_x)Cr_1$, x=0, 0.2, 0.4, J. Alloys Compd. 767 (2018) 432–438.
[23] B. Hosni, C. Khaldi, O. ElKedim, N. Fenineche, J. Lamloumi, Structure and electrochemical hydrogen storage properties of Ti-Fe-Mn alloys for Ni-MH accumulator applications, J. Alloys Compd. 781 (2019) 1159–1168.
[24] Y. Yan, Y. Chen, H. Liang, C. Wu, M. Tao, The effect of Si on $V_{30}Ti_{35}Cr_{25}Fe_{10}$ BCC hydrogen storage alloy, J. Alloys Compd. 441 (2007) 297–300.
[25] L. Ouyang, J. Huang, H. Wang, J. Liu, M. Zhu, Progress of hydrogen storage alloys for Ni-MH rechargeable power batteries in electric vehicles: a review, Mater. Chem. Phys. 200 (2017) 164–178.
[26] K. Young, J. Nei, D. Wong, L. Wang, Structural, hydrogen storage, and electrochemical properties of Laves phase-related body-centered-cubic solid solution metal hydride alloys, Int. J. Hydrogen Energy 39 (2014) 21489–21499.
[27] L. Wang, K. Young, J. Nei, D. Pawlik, K. Ng, Hydrogenation of $AB_5$ and $AB_2$ metal hydride alloys studied by in situ X-ray diffraction, J. Alloys Compd. 616 (2014) 300–305.
[28] S. Tan, Y. Shen, E. Onur Şahin, D. Noréus, T. Öztürk, Activation behavior of an $AB_2$ type metal hydride alloy for NiMH batteries, Int. J. Hydrogen Energy 41 (2016) 9948–9953.
[29] Y. Zhang, J. Li, T. Zhang, H. Kou, X. Xue, Hydrogen absorption properties of a non-stoichiometric Zr-based Laves alloy against gaseous impurities, Int. J. Hydrogen Energy 42 (2017) 10109–10116.
[30] K. Young, B. Reichman, M. Fetcenko, Electrochemical performance of $AB_2$ metal hydride alloys measured at– 40 °C, J. Alloys Compd. 580 (2013) S349–S352.
[31] M. Yoshida, E. Akiba, Hydrogen absorbing-desorbing properties and crystal structure the Zr-Ti-Ni-Mn-V $AB_2$ Laves phase alloys, J. Alloys Compd. 224 (1995) 121–126.
[32] A.C. Larson, R.B.V. Dreele, Los Alamos National Laboratory Report LANR, 2004, p. 86.
[33] V.V. Burnasheva, V.A. Yartys, N.V. Fadeeva, S.P. Solov'ev, K.N. Semenenko, Neutron diffraction investigation of the $LaNiD_{3.7}$ deuteride, Russ. J. Inorg. Chem. 27 (1982) 1112–1116.
[34] K. Young, D.F. Wong, T. Ouchi, B. Huang, B. Reichman, Effects of La-addition to the structure, hydrogen storage, and electrochemical properties of C14 metal hydride alloys, Electrochim. Acta 174 (2015) 815–825.
[35] K. Young, B. Chao, D. Pawlik, H. Shen, Transmission electron microscope studies in the surface oxide on the La-containing $AB_2$ metal hydride alloy, J. Alloys Compd. 672 (2016) 356–365.
[36] A.A. Volodin, R. Denys, G. Tsirlina, B. Tarasov, M. Fichtner, V. Yartys, Hydrogen diffusion in $La_{1.5}Nd_{0.5}MgNi_9$ alloy electrodes of the Ni/MH battery, J. Alloys Compd. 645 (2015) S288–S291.
[37] A.A. Volodin, C. Wan, R.V. Denys, G.A. Tsirlina, B.P. Tarasov, M. Fichtner, U. Ulmer, Y. Yu, C.C. Nwakwuo, V.A. Yartys, Phase-structural transformations in a metal hydride battery anode $La_{1.5}Nd_{0.5}MgNi_9$ alloy and its electrochemical performance, Int. J. Hydrogen Energy 41 (2016) 9954–9967.
[38] S. Yang, S. Han, Y. Li, J. Liu, Study on the microstructure and electrochemical kinetic properties of $MmNi_{4.50-x}Mn_xCo_{0.45}Al_{0.30}$ ($0.25 \leq x \leq 0.45$) hydrogen storage alloys, Mater. Sci. Eng. B 178 (2013) 39–44.
[39] W. Hu, R.V. Denys, C. Nwakwuo, T. Holm, J.P. Maehlen, J.K. Solberg, V.A. Yartys, Annealing effect on phase composition and electrochemical properties of the Co-free $La_2MgNi_9$ anode for Ni-Metal Hydride batteries, Electrochim. Acta 96

(2013) 27–33.
[40] M. Latroche, F. Cuevas, W. Hu, D. Sheptyakov, R.V. Denys, V.A. Yartys, Mechanistic and kinetic study of the electrochemical charge and discharge of $La_2MgNi_9$ by in situ powder neutron diffraction, J. Phys. Chem. C 118 (2014) 12162–12169.
[41] I.E. Gabis, E.A. Evard, A.P. Voyt, V.G. Kuznetsov, B.P. Tarasov, J.-C. Crivello, M. Latroche, R.V. Denys, W. Hu, V.A. Yartys, Modeling of metal hydride battery anodes at high discharge current densities, Electrochim. Acta 147 (2014) 73–81.
[42] V. Yartys, D. Noreus, M. Latroche, Metal hydrides as negative electrode for Ni-MH batteries, Appl. Phys. A 122 (2016) 43.
[43] C. Wan, R.V. Denys, V.A. Yartys, In situ neutron powder diffraction study of phase-structural transformations in La-Mg-Ni battery anode alloy, J. Alloys Compd. 670 (2016) 210–216.
[44] N.S. Nazer, R.V. Denys, V.A. Yartys, W. Hu, M. Latroche, F. Cuevas, B.C. Hauback, P.F. Henry, L. Arnberg, In operando neutron diffraction study of LaNd-$MgNi_9H_{13}$ as a metal hydride battery anode, J. Power Sources 343 (2017) 502–512.
[45] K. Young, T. Ouchi, J. Nei, D. Moghe, The importance of rare-earth additions in Zr-based $AB_2$ metal hydride alloys, Batteries 2 (2016) 25.
[46] C. Wan, R. Denys, M. Lelis, D. Milčius, V. Yartys, Electrochemical studies and phase-structural characterization of a high-capacity La-doped $AB_2$ Laves type alloy and its hydride, J. Power Sources 418 (2019) 193–201.
[47] X. Li, H. Dong, A. Zhang, Y. Wei, Electrochemical impedance and cyclic voltammetry characterization of a metal hydride electrode in alkaline electrolytes, J. Alloys Compd. 426 (2006) 93–96.
[48] G.H. Ağaoğlu, G. Orhan, Elaboration and electrochemical characterization of Mg–Ni hydrogen storage alloy electrodes for Ni/MH batteries, Int. J. Hydrogen Energy 42 (2017) 8098–8108.
[49] X. Yuan, N. Xu, Determination of hydrogen diffusion coefficient in metal hydride electrode by modified Warburg impedance, J. Alloys Compd. 329 (2001) 115–120.
[50] S. Malifarge, B. Delobel, C. Delacourt, Determination of tortuosity using impedance spectra analysis of symmetric cell, J. Electrochem. Soc. 164 (2017) E3329–E3334.
[51] P. De Vidts, J. Delgado, R.E. White, Mathematical modeling for the discharge of a metal hydride electrode, J. Electrochem. Soc. 142 (1995) 4006–4013.
[52] J. Backholm, P. Georén, G.A. Niklasson, Determination of solid phase chemical diffusion coefficient and density of states by electrochemical methods: application to iridium oxide-based thin films, J. Appl. Phys. 103 (2008), 023702.
[53] M.D. Levi, C. Wang, D. Aurbach, Two parallel diffusion paths model for interpretation of PITT and EIS responses from non-uniform intercalation electrodes, J. Electroanal. Chem. 561 (2004) 1–11.